PERGAMON

International Journal of Heat and Mass Transfer 45 (2002) 1077–1091

International Journal of HEAT and MASS TRANSFER

www.elsevier.com/locate/ijhmt

Metal droplet deposition on non-flat surfaces: effect of substrate morphology

A.M. Ahmed, R.H. Rangel *

Department of Mechanical and Aerospace Engineering, University of California, Irvine, CA 92697-3975, USA

Received 3 April 2001; received in revised form 31 May 2001

Abstract

In droplet-based deposition processes, substrate morphology plays an important role in the bonding quality between splats and substrate. This paper presents a numerical investigation of metal droplet impact and solidification on two types of non-flat surfaces, namely a pre-molten pool and a wavy surface. We solve the axi-symmetric incompressible Navier–Stokes equations and an enthalpy formulation of the energy equation to simulate both the flow field and the heat transfer during droplet spreading and solidification. The results show that for efficient droplet deposition on molten pools, the pool size and droplet impact velocity should be kept relatively small. Droplet impingement on non-flat surfaces is almost always accompanied by splashing. The degree of splashing decreases with the increase in surface roughness height. Increasing surface roughness wavelength improves droplet spreading and hence solidification.

1. Introduction

Thermal spray deposition is a manufacturing process for the production of materials that exhibit certain desired characteristics. These include the production of fine-grained microstructures as a result of rapid solidification [1]. In micro-casting and in free-form manufacturing, near net-shaped structures are produced [2]. It is well-known that the properties of the resulting structure, such as porosity, surface roughness and adhesion strength of coatings depend on droplet properties such as velocity, size and temperature as well as substrate conditions [3]. Thus, in order to maximize the efficiency of a metal droplet deposition process, it is necessary to develop a thorough understanding of the interrelation of these parameters as well as the nature of the physical phenomena that are involved.

In the pursuit of understanding of the complex phenomena involved in thermal spray deposition processes, a large number of analytical, experimental and numerical studies have taken place over the past few decades. Some of these studies concentrated on the effect of the nature of the substrate on resulting quality of the formed splats. Mundo et al. [4] conducted an experimental study of the deformation and breakup of droplets on both smooth and rough substrates. They concluded that, in the case of droplet impact on a smooth surface, splashing occurs due to the decay of a cylindrical sheet ('corona') that arises around the point of impingement. On the other hand, for droplet impact on a rough surface (roughness in the order of the diameter of the primary droplet), splashing occurs without the formation of splash-corona. The occurrence of droplet splash or deposition depends, among others, on the fluid properties and kinematic impact parameters. Liu et al. [5] conducted a numerical study of molten droplet impingement on a non-flat surface. They studied different droplet substrate configurations without solidification. They found out that when the wavelength of the wavy surface was larger than the droplet diameter, droplet spreading exhibited periodic repetition of acceleration–deceleration behavior that ended with a droplet break up.

* Corresponding author. Tel.: +1-949-824-4033; fax: +1-949-824-8585.

E-mail address: rhrangel@uci.edu (R.H. Rangel).

0017-9310/02/$ - see front matter
PII: S0017-9310(01)00198-3

Nomenclature

F	volume-of-fluid function
$\mathbf{F}_b$	body forces
g	gravity acceleration
h	specific enthalpy
H	enthalpy per unit volume
h_p	molten pool maximum depth
K	heat conductance
p	pressure
$\mathbf{q}$	heat flux
R_p	molten pool radius
t	time
$\mathbf{V}$	velocity vector

Greek symbols

ε	non-dimensional surface roughness height
λ	non-dimensional surface roughness wavelength
θ	volume fraction open to flow
ρ	density
τ	viscous stress tensor

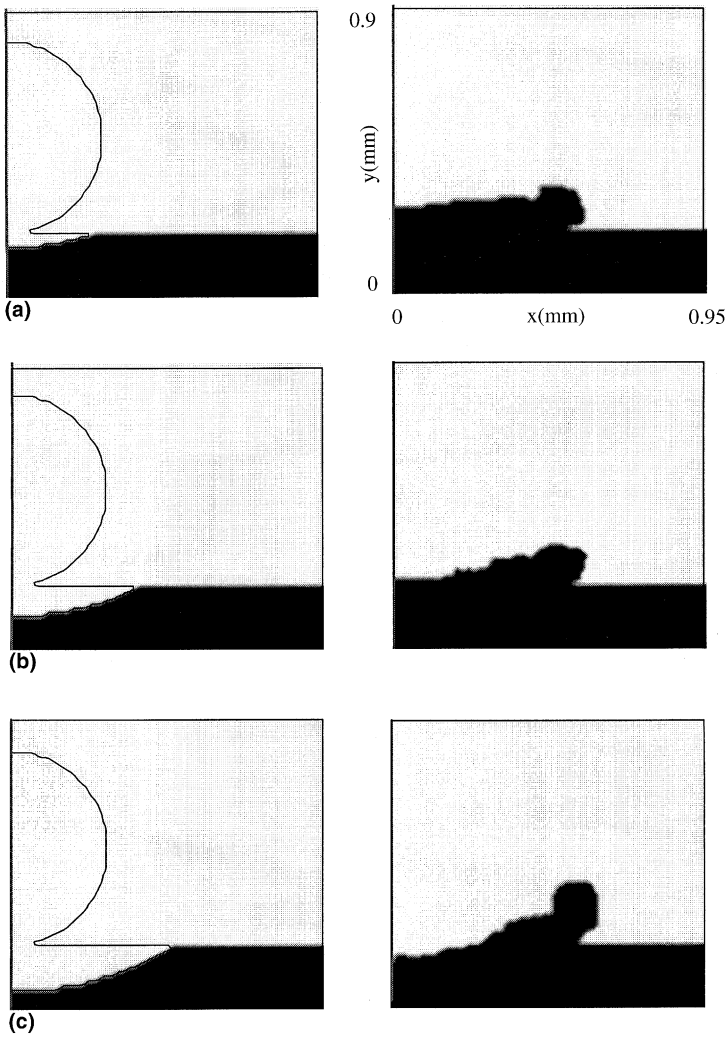

Fig. 1. Initial and final configurations of droplet impingement on three molten pool sizes. (a) Case I ($R_p = 287$ μm, $h_p = 50$ μm). (b) Case II ($R_p = 412$ μm, $h_p = 100$ μm). (c) Case III ($R_p = 512$ μm, $h_p = 150$ μm).

One objective of this study is to consider the effect of surface roughness on the quality of formed splat in thermal spray processes. A second objective is to investigate the possibility of improving the bonding quality between a spreading droplet and a substrate by pre-melting the substrate at the point of impact. These

two situations are representative of a wide variety of non-flat substrate conditions encountered in practice.

2. Numerical simulation

The problem involves the numerical simulation of droplet impingement on either a molten pool or on a non-flat surface. The fluid dynamics is simulated based on a method developed by Kothe et al. [6]. We upgraded this methodology to include heat transfer and phase change to allow for the existence of solidifying fronts. The heat transfer and solidification are simulated using an enthalpy formulation of the energy equation. The droplets are assumed spherical at the moment of impact, are initially in the molten state with uniform velocity and temperature fields.

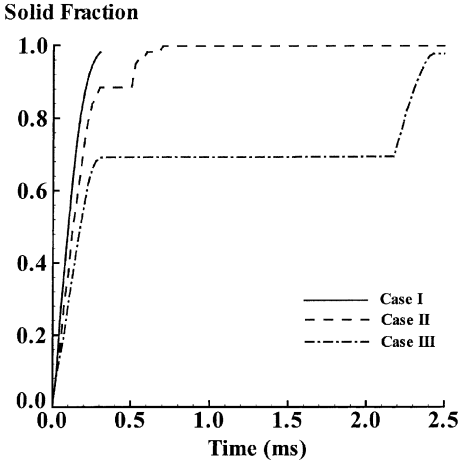

Fig. 2. Time evolution of the solid fraction for droplet impingement on three molten pools. Cases labeled as in Fig. 1.

The velocity field inside the spreading droplet with a free surface is described using the two-dimensional, axisymmetric, incompressible Navier–Stokes equations:

$$\nabla \cdot (\theta \mathbf{V}) = 0, \tag{1}$$

$$\theta \frac{\partial \mathbf{V}}{\partial t} + \nabla \cdot (\theta \mathbf{V}\mathbf{V}) = -\frac{\theta}{\rho}\nabla p + \frac{\theta}{\rho}\nabla \cdot \tau + \theta g + \theta \mathbf{F}_{\mathrm{b}}, \tag{2}$$

where θ is a characteristic function ($\theta = 0$ in the solid and $\theta = 1$ in the liquid) used to describe the effect of growing solidification on the flow field. Cells that are partially solid are described by a value of θ in the range $0 < \theta < 1$ (θ is then an average value over the cell). The free surface of the spreading droplet is calculated using the volume-of-fluid transport equation:

$$\frac{\partial}{\partial t}(\theta F) + \nabla \cdot (\theta F \mathbf{V}) = 0, \tag{3}$$

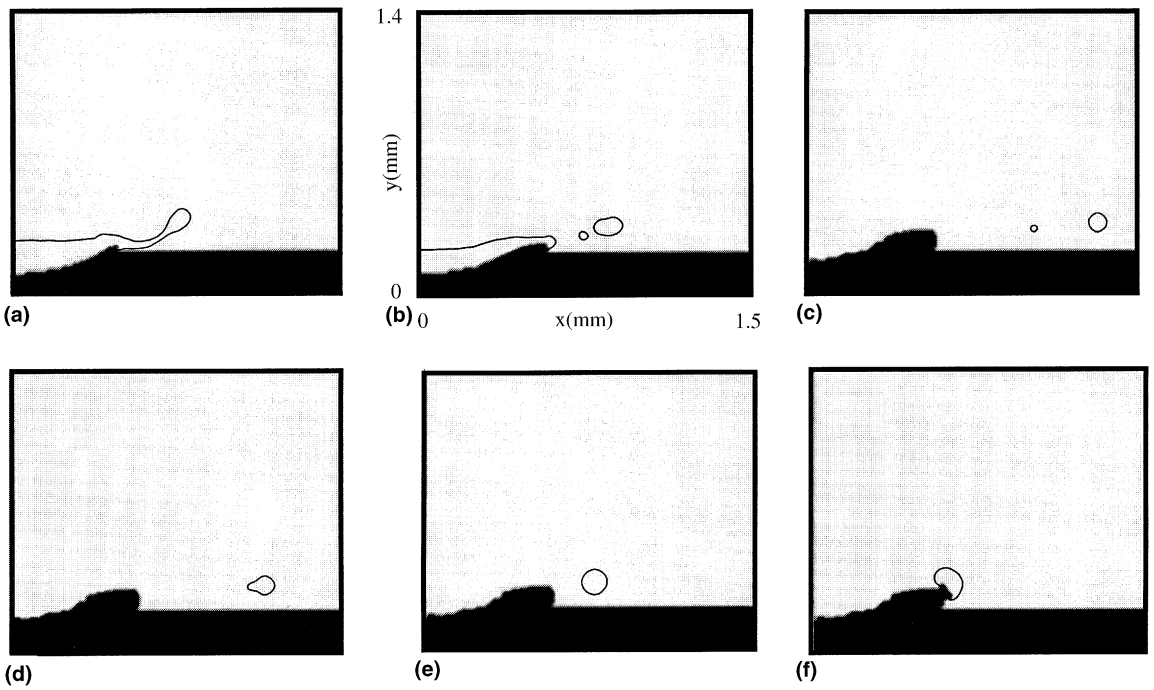

Fig. 3. Time sequence for droplet impact of case III when initial droplet velocity is 10 m/s.

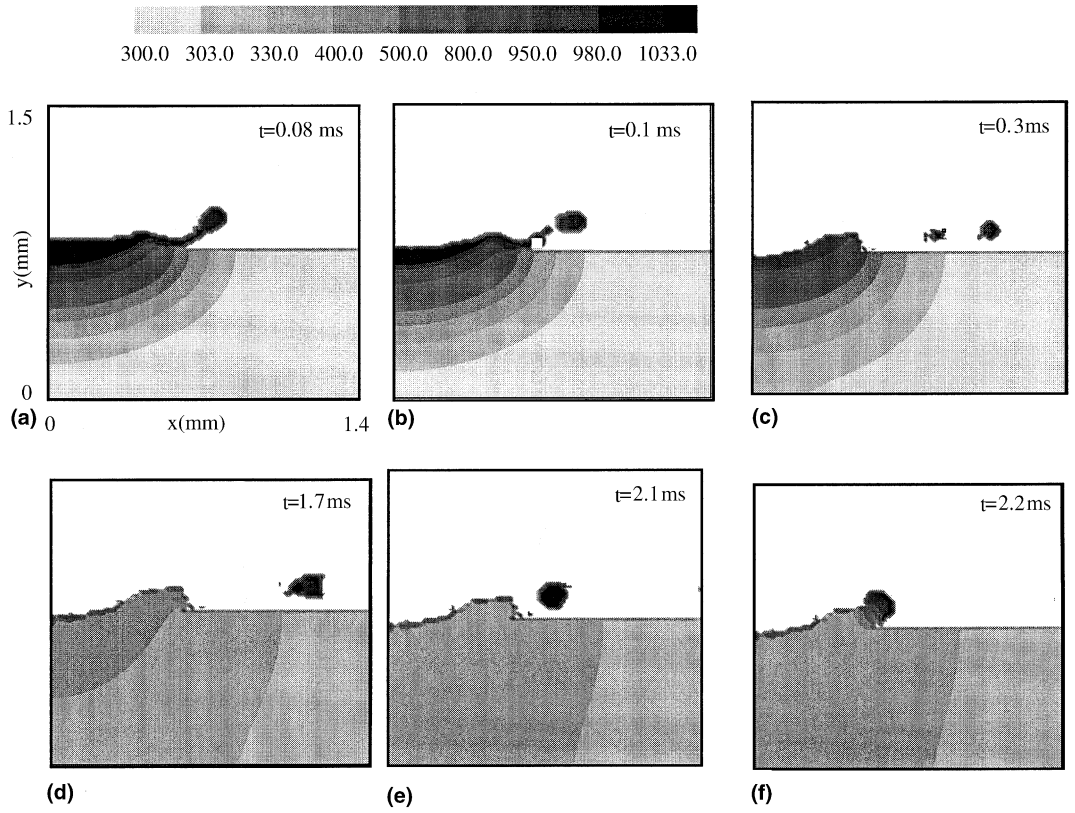

Fig. 4. Temperature evolution for the droplet impact of case III with droplet impact velocity of 10 m/s.

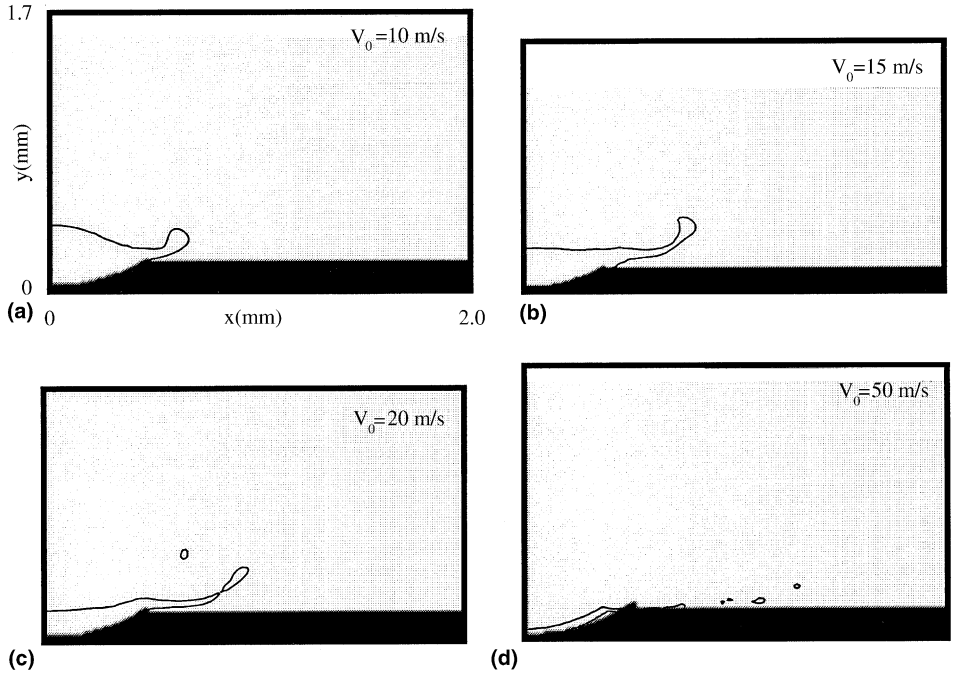

Fig. 5. Effect of initial droplet velocity for case III at $t = 0.05$ ms. (a) $V_0 = 10$ m/s, (b) $V_0 = 15$ m/s, (c) $V_0 = 20$ m/s and (d) $V_0 = 50$ m/s.

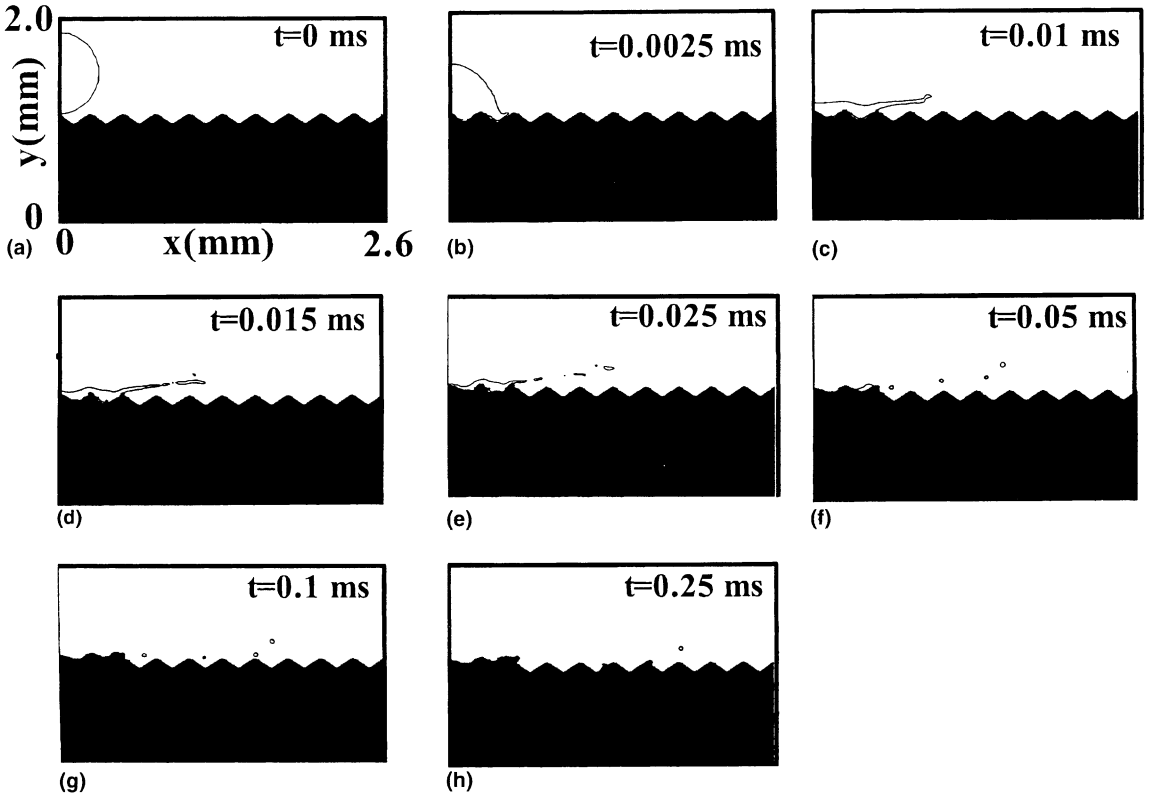

Fig. 6. Time sequence when a 600 μm droplet impinges on a wavy substrate at a speed of 100 m/s for $\lambda = 0.4$ and $\varepsilon = 0.11$.

where F is the volume of fluid function ($F = 1$ in the liquid, $F = 0$ in the void). A cell that is partially filled is described by a value of F in the range $0 < F < 1$ (F is then an average value over the cell). Surface tension effects are described using the continuum surface force approach [7]. Details of the numerical procedure may be found in the work by Kothe et al. [6].

The enthalpy formulation of the thermal energy conservation law for an incompressible fluid can be written as:

$$\frac{\partial \rho h}{\partial t} + \nabla \cdot (\rho \mathbf{V} h) = -\nabla \cdot \mathbf{q}. \tag{4}$$

At low to moderate impingement velocities (a few hundred m/s at most), the heat generated by viscous dissipation is negligible [8]. The advection term in (4) is evaluated using a second-order upwind, weakly monotonic scheme [6]. The divergence term on the RHS of (4) is calculated using a conservative formulation by evaluating it over the surface of the control volume used in the numerical integration.

2.1. Discretization

The final from of the discretized enthalpy equation (4) is

$$\begin{aligned} H_{i,j}^{n+1} = H_{i,j}^{n} &- \frac{\Delta t^n}{r_i^{\delta} \Delta x_i}\left[r_{i+1/2}^{\delta} q_{i+1/2,j}^{n} - r_{i-1/2}^{\delta} q_{i-1/2,j}^{n}\right] \\ &- \frac{\Delta t^n}{\Delta y_j}\left[q_{i,j+1/2}^{n} - q_{i,j-1/2}^{n}\right] \frac{\Delta t^n}{r_i^{\delta} \Delta x_i}\left[r_{i+1/2}^{\delta} u_{i+1/2,j}^{n+1} \langle H \rangle_{\mathrm{R}}^{n}\right. \\ &\left. - r_{i-1/2}^{\delta} u_{i-1/2,j}^{n+1} \langle H \rangle_{\mathrm{L}}^{n}\right] - \frac{\Delta t^n}{\Delta y_j}\left[v_{i,j+1/2}^{n+1} \langle H \rangle_{\mathrm{T}}^{n}\right. \\ &\left. - v_{i,j-1/2}^{n+1} \langle H \rangle_{\mathrm{B}}^{n}\right], \end{aligned} \tag{5}$$

where the superscript $(n+1)$ refers to the new time and (n) is the old time. The superscript δ over the radius r is equal to 1 in cylindrical coordinates and 0 in Cartesian coordinates. $H_{i,j}^{n} = (\rho h)_{i,j}^{n}$ is the density times enthalpy evaluated at the point with coordinates (i, j) at time level n. Δt is the time increment, Δx is the discretization control volume spacing in the

x-direction and Δy is the control volume spacing in the y-direction. The subscripts T, B, R and L denote quantities evaluated at the top, bottom, right and left, respectively, of a cell (i, j).

In Eq. (5) the heat flux $q^n_{i+1/2,j}$ is evaluated as

$$q^n_{i+1/2,j} = -K^n_{i+1/2,j}(T^n_{i+1,j} - T^n_{i,j}), \tag{6}$$

where $K^n_{i+1/2,j}$ is a conductance that satisfies flux continuity [9] and is given by

$$K^n_{i+1/2,j} = \left[\frac{x_{i+1/2} - x_i}{k^n_{i,j}} + \frac{x_{i+1} - x_{i+1/2}}{k^n_{i+1,j}}\right]^{-1}. \tag{7}$$

Other heat fluxes are evaluated in a similar way. The bracketed quantities $\langle H \rangle$ are the enthalpies evaluated at each cell boundary.

2.2. Boundary conditions

The problem considered is treated as axi-symmetric and thus a symmetry boundary condition is used along the axis in the computational domain. The computational domain is extended axially to allow an impacted droplet to solidify on the substrate. However, it was not possible to extend it indefinitely to account for all the splashed fluid blobs. A no-slip boundary condition is used at the contact points between liquid and solid. Thermal contact resistance is neglected. Heat transfer to the ambient above the substrate is neglected. On the solidification front, cells that reach the solidification temperature are considered closed to flow, but continue to loose latent heat to its surroundings until they solidify completely.

3. Results and discussion

As base cases, we considered the impact of a 600 μm diameter droplet with different velocities for both substrate conditions. For the molten pool case, the droplet velocity is limited to a maximum of 50 m/s. At this velocity, there is significant droplet splashing which increases with increasing droplet speed. On the other hand, for the wavy surface case, the maximum droplet impact velocity is set at 400 m/s. The droplet at impact is a superheated liquid with a 100° of su-

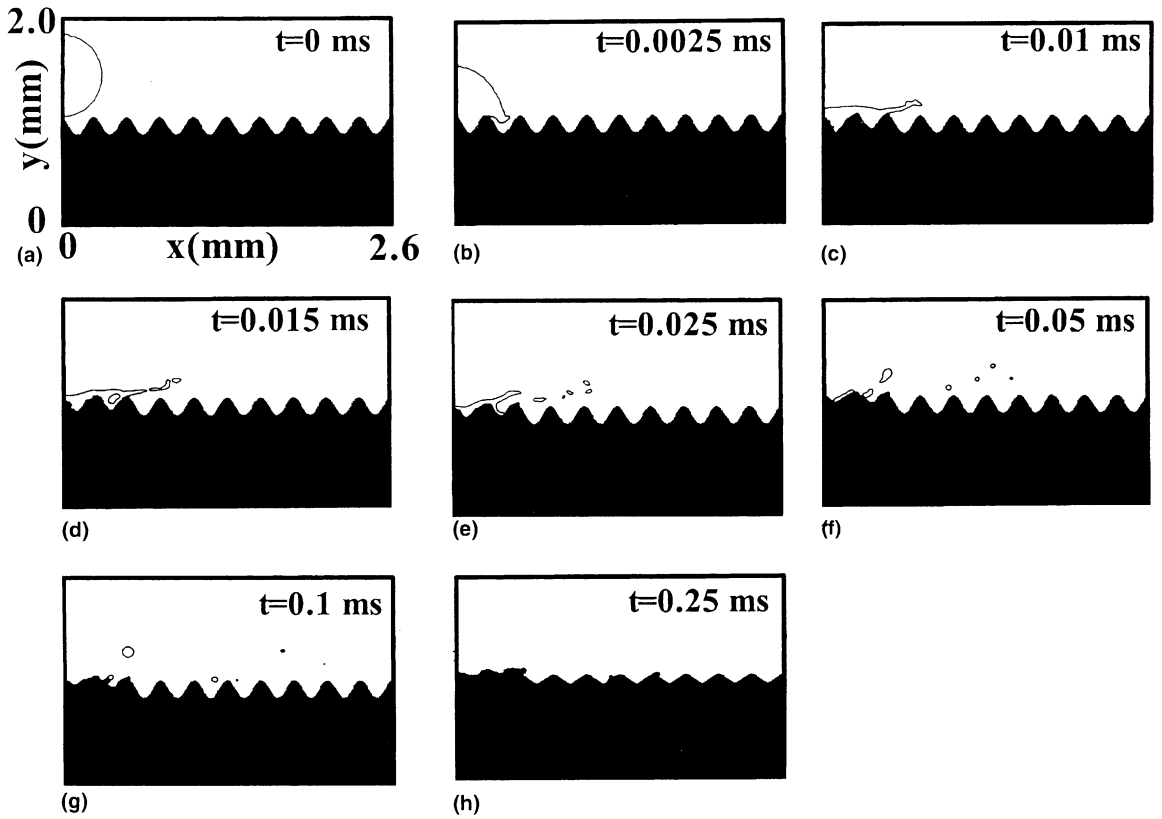

Fig. 7. Time sequence when a 600 μm droplet impinges on a wavy substrate at a speed of 100 m/s for $\lambda = 0.4$ and $\varepsilon = 0.22$.

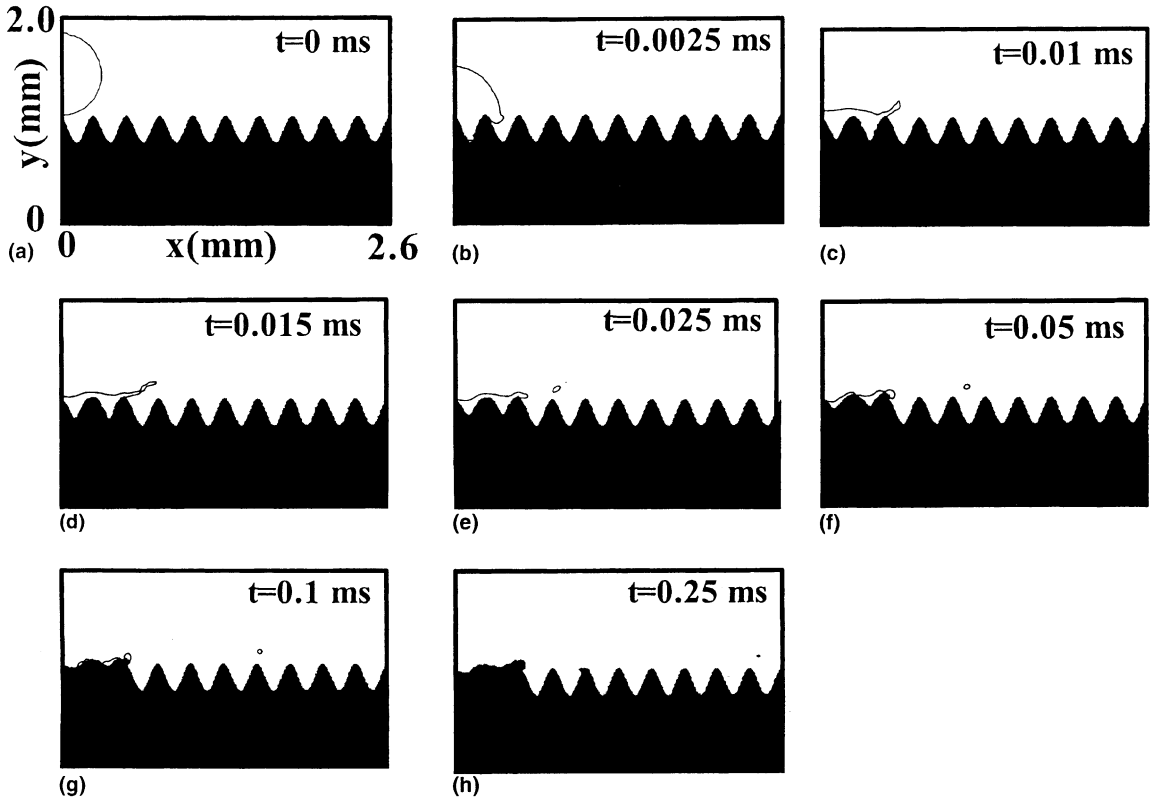

Fig. 8. Time sequence when a 600 μm droplet impinges on a wavy substrate at a speed of 100 m/s for $\lambda = 0.4$ and $\varepsilon = 0.33$.

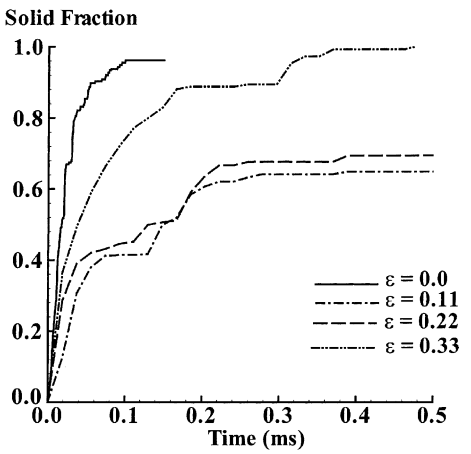

Fig. 9. Effect of the substrate roughness amplitude on the time development of the solid fraction for $\lambda = 0.4$.

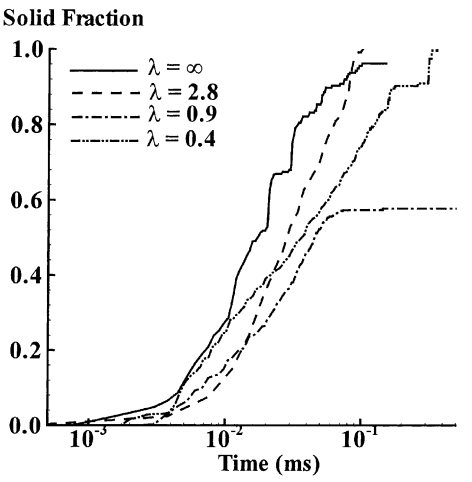

Fig. 10. Effect of the substrate roughness wavelength on the time development of the solid fraction for $\varepsilon = 0.33$.

perheat. The non-flat substrate is initially at room temperature (300 K), while the molten pool is initially at the melting temperature. The liquid metal in the pool is initially stagnant. We used aluminum metal for both the droplet and the substrate for all the cases studied. Grid independence tests proved that a non-uniform grid size of 200×120 was sufficient for converged results.

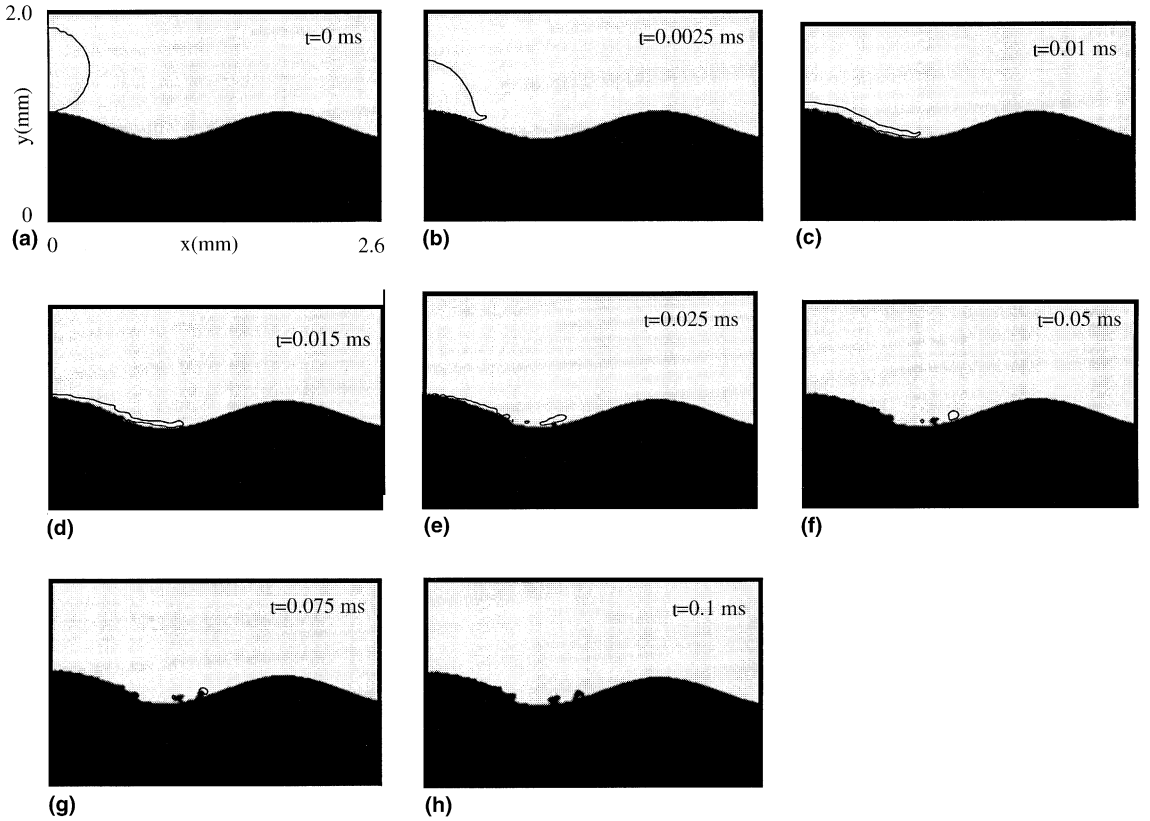

Fig. 11. Time sequence when a 600 μm droplet impinges on a wavy substrate at a speed of 100 m/s for $\lambda = 2.8$ and $\varepsilon = 0.33$.

3.1. Impact on a molten pool

We studied three configurations of molten pools. These configurations will be referred to as case I ($R_p = 287$ μm, $h_p = 50$ μm), case II ($R_p = 412$ μm, $h_p = 100$ μm), and case III ($R_p = 512$ μm, $h_p = 150$ μm), in order of increasing pool size. For each case, we used four different impinging velocities, namely $V_0 = 10$, 15, 20 and 50 m/s. The initial and final configurations for droplet impact at 10 m/s on the three pools are shown in Fig. 1. The figure shows that the curvature of the solidified splat (upward concavity) tends to be more pronounced as the pool size increases. This upward concavity is directly related to the shape of the molten pool. As the pool size increases, a larger liquid mass is available for flow ejection under the effect of the kinetic energy of the incoming droplet. This ejected volume solidifies forming the concave surface.

Fig. 2 shows the time evolution of the solid fraction for the three configurations described above. It is seen that as the pool size increases, the time taken for complete solidification increases. However, in case III, the solid fraction does not change between $t \approx 0.3$ ms and $t \approx 2.2$ ms. The reason for this behavior can be explained by reference to Fig. 3. Fig. 3(a) shows the time at which splashing is about to take place ($t \approx 0.08$ ms). Fig. 3(b) shows two ring ligaments that are formed by splashing at $t \approx 0.1$ ms. The two rings subsequently move away from the molten pool and apart from each other as seen in Fig. 3(c). They continue to move away from the molten pool reaching a maximum separation, after which they move back towards the molten pool (due to surface tension effects) where they merge to form a single ring as seen in Fig. 3(d). The newly formed ring continues to move inward towards the solidified molten pool under the effect of surface tension (Fig. 3(e)), and it eventually reaches the solidified splat where it begins to solidify at $t \approx 2.2$ ms as seen in Fig. 3(f). Fig. 4 shows the temperature evolution for the case shown in Fig. 3.

Fig. 5 shows the effect of increasing the droplet impact velocity for configuration III. The figure shows the situation at $t = 0.05$ ms after impact. When the initial droplet velocity is 10 m/s (Fig. 5(a)), the fluid is just developing its upward concavity near the rim of the droplet. When the droplet velocity is increased to 15 m/s (Fig. 5(b)), the concave surface is further developed and

is about to break up. By increasing the droplet velocity to 20 m/s (Fig. 5(c)), the droplet breaks up and forms two satellite rings. As the droplet velocity is increased to 50 m/s (Fig. 5(d)), many rings of different sizes are formed.

3.2. Impact on an uneven substrate

In this section, we present results for droplet impingement on an uneven substrate. To model and quantify the *roughness*, these surfaces are represented as sinusoidal functions with a wavelength λ and amplitude ε, both normalized by the droplet diameter. In our results, we varied the amplitude ε from 0 to 0.33 and the wavelength λ from 0.4 to 2.8. We also varied the droplet impingement velocity from 50 to 400 m/s. Two configurations for the sinusoidal functions are considered. First, we consider the case when the drop impinges on the crest of the wave and then we compare these results with those of the case when the drop impinges on the valley of the wave. These situations represent the two extremes that can be studied with an axi-symmetric model.

3.3. Droplet impact on a crest

Fig. 6 shows the temporal development during droplet spreading on the uneven substrate with $\varepsilon = 0.11$ and $\lambda = 0.4$. The figure shows that the droplet initially fills the first two valleys of the wavy surface, and that this is followed first by jetting and finally by splashing. Some of the fluid solidifies while some of the splashed fluid leaves the computational domain. Fluid jetting takes place as a result of the deflection of the impinging droplet fluid by the upward curvature of the wavy surface. After the deflected fluid layer becomes thin enough for the fluid kinetic energy to overcome the surface tension forces, the droplet breaks up into annular blobs. These blobs eventually reach the substrate where they solidify.

Fig. 7 shows the temporal development during droplet spreading on the uneven substrate with $\varepsilon = 0.22$ and $\lambda = 0.4$. It is seen that a similar mechanism, as described in regard to Fig. 6, takes place. However, jetting action is reduced as can be seen from comparing Fig. 6(c) and (d) with Fig. 7(c) and (d). This is due to the increased surface roughness height, as more fluid is used

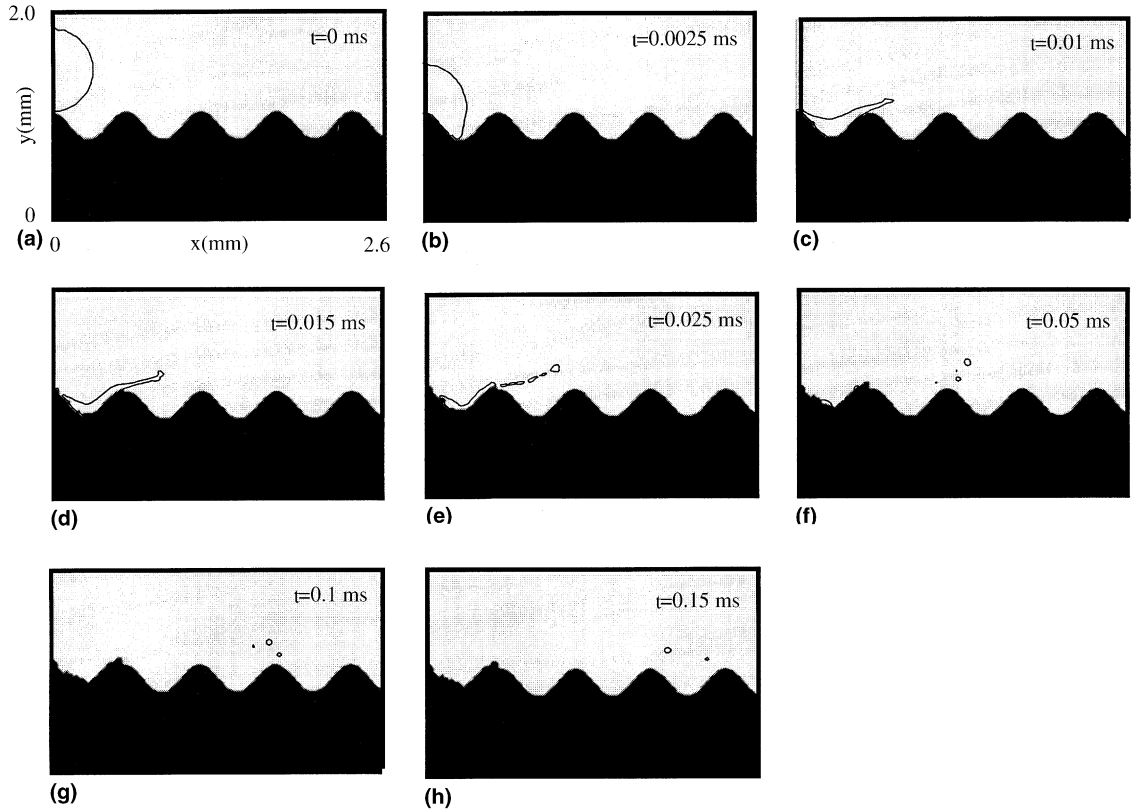

Fig. 12. Time sequence when a 600 μm droplet impinges on a wavy substrate at a speed of 100 m/s for $\lambda = 0.9$ and $\varepsilon = 0.33$.

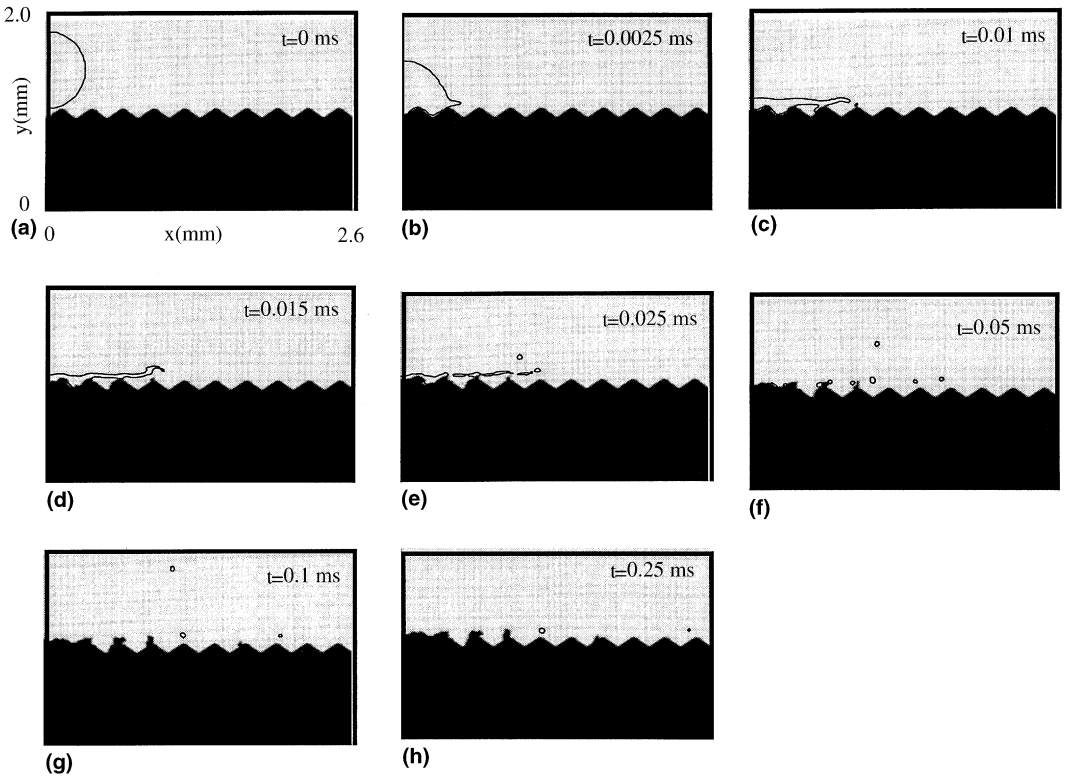

Fig. 13. Time sequence when a 600 μm droplet impinges on the valley of a wavy substrate at a speed of 100 m/s for $\lambda = 0.4$ and $\varepsilon = 0.11$.

to fill in the deeper valleys, and consequently less fluid is available for jetting. The exit of some splashed fluid from the computational domain reduces the solid fraction as will be shown later on.

Fig. 8 shows the temporal development during droplet spreading on the wavy substrate with $\varepsilon = 0.33$ and $\lambda = 0.4$. Similar behavior is seen in this case as in the two earlier cases. However, due to the increased height of the surface roughness, more fluid is retained in the valleys leading to a significant reduction in jetting and splashing. This is reflected in the increased rate of solidification corresponding to this case as compared to that for the previous two cases, as illustrated in Fig. 9. This figure shows the temporal development of the solid fraction for the three cases presented in Figs. 6–8. In addition, another case with $\varepsilon = 0$ (flat substrate) is shown for comparison. The figure shows, as expected, that the droplet solidifies faster on a flat substrate ($\varepsilon = 0$). As ε increases, the rate of solidification decreases (compare the case with $\varepsilon = 0.11$ to that with $\varepsilon = 0$). The case with $\varepsilon = 0.33$ results in faster solidification than that with $\varepsilon = 0.22$, as discussed earlier. Those cases for which the solid fraction does not reach unity are the result of some of the splashed blobs leaving the computational domain.

We now investigate the effect of the wavelength λ by considering a 600 μm diameter droplet with an impact velocity of 100 m/s. Three cases are analyzed, with λ taking the values 0.4, 0.9 and 2.8 while ε is kept constant at 0.33. Fig. 10 shows the temporal development of the solid fraction for these three cases. The figure shows that the case with the longest wavelength ($\lambda = 2.8$) results in the fastest solidification time. On the other hand, the case with the smallest wavelength considered ($\lambda = 0.4$) solidifies faster than the case with the intermediate wavelength ($\lambda = 0.9$). The reason for this behavior can be explained by examining the solidification patterns for these cases as seen in Figs. 8, 11 and 12. The presence of the surface roughness significantly alters the qualitative evolution of the spreading process. During the early stages ($t = 2.5$ μs), the increased contact area brought about by a reduction in wavelength, enhances the rate of solidification. For longer wavelengths, the formation of a lip near the droplet rim, as seen in Fig. 11(b), is more pronounced. This is related to the mechanism of liquid jet overflow produced by the transfer of vertical

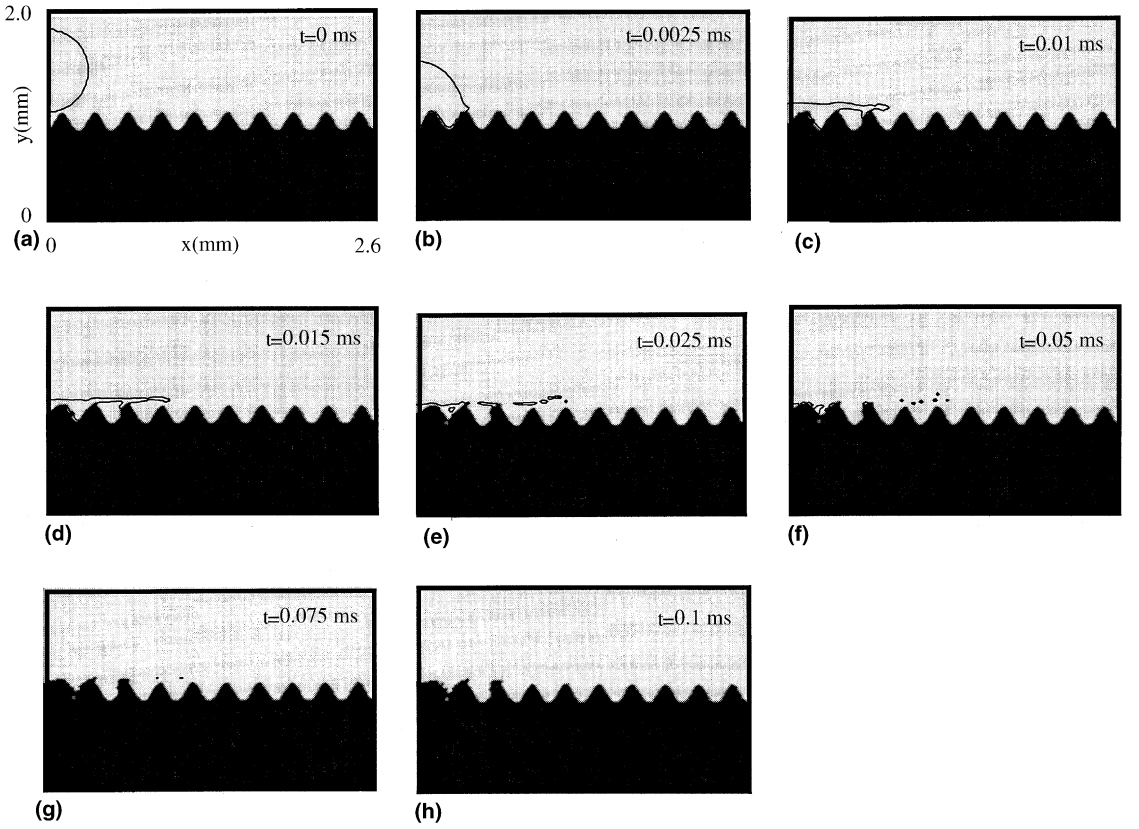

Fig. 14. Time sequence when a 600 μm droplet impinges on the valley of a wavy substrate at a speed of 100 m/s for $\lambda = 0.4$ and $\varepsilon = 0.22$.

momentum to radial momentum, described by Delplanque et al. [10].

Fig. 11 shows the temporal development for the case with $\lambda = 2.8$ and $\varepsilon = 0.33$. The figure shows that the fluid spreads smoothly on the substrate until it becomes thin enough that the kinetic energy overcomes the surface tension force leading to the breakup of the fluid layer into small annular blobs. These blobs solidify separately on the substrate forming a discontinuous solidified splat. The larger solidification rate for this case seen in Fig. 10 is due to the relative smoothness of this substrate compared to the ones with smaller λ which tend to produce more splashing.

Fig. 12 shows the temporal development for the case with $\lambda = 0.9$ and $\varepsilon = 0.33$. It can be seen that as λ is reduced in comparison to the previous cases, the droplet solidification pattern becomes similar to that in Fig. 8 ($\lambda = 0.4$ and $\varepsilon = 0.33$), due to the increase in slope associated with a decrease in λ. The difference between these two cases is that for $\lambda = 0.9$, the fluid is only able to fill one valley. Since some of the splashed fluid leaves the computational domain, the solid fraction does not reach unity in this case (Fig. 10).

3.4. Droplet impact on a valley

The results for this case are shown in Figs. 13–19. Figs. 13–15 show for impact on a valley should be contrasted with Figs. 6–8 for impact on a crest. The figures show the effect of increasing surface roughness amplitude in an increasing order from 0.11 to 0.33. It is seen that the droplet fluid fills the first two valleys of the wavy surface before it begins to jet and splash. Fig. 16 shows the solid fraction evolution for the cases shown in Figs. 13–15 for impact on a valley and also for those in Figs. 6–8 for impact on a crest. The curves representing cases for impact on a crest (Figs. 6–8) are drawn with thick lines, while those representing cases for impact on a valley (Figs. 13–15) are drawn with thin lines. Fig. 16 shows that the droplet spreading on a flat substrate has the highest rate of solidification. However, a relatively small amount of surface roughness results in significant splashing and consequently a

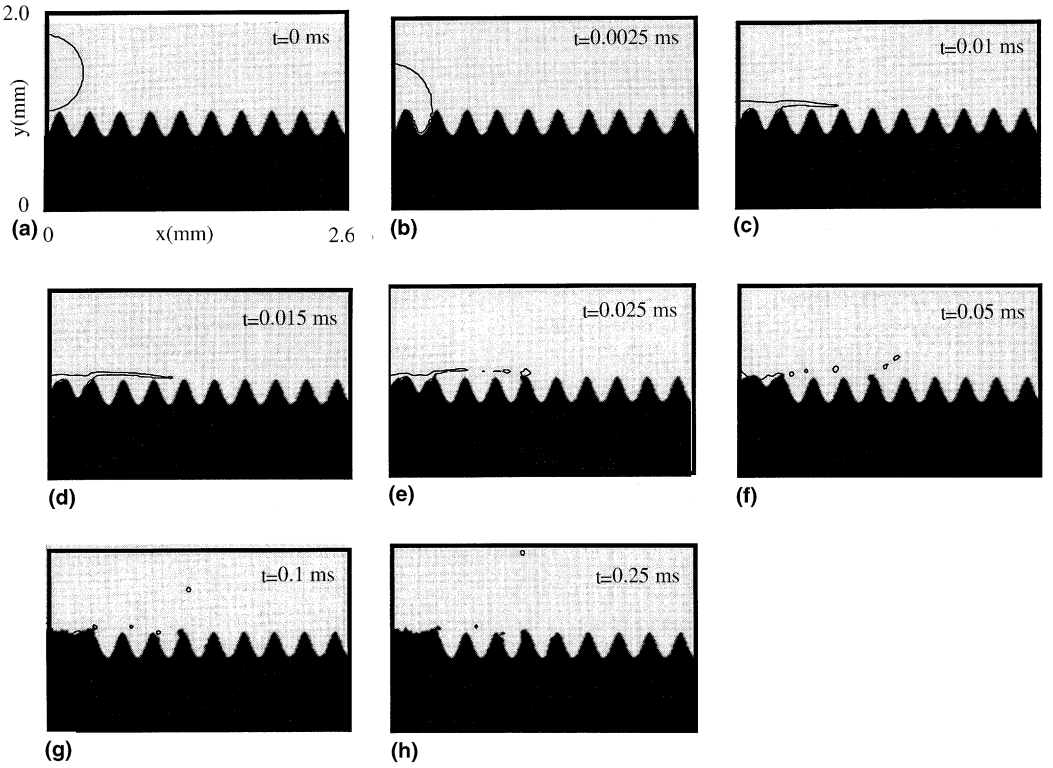

Fig. 15. Time sequence when a 600 μm droplet impinges on the valley of a wavy substrate at a speed of 100 m/s for $\lambda = 0.4$ and $\varepsilon = 0.33$.

significantly reduced solidification rate ($\varepsilon = 0.11$). When the roughness is increased further, the splashing is reduced as more liquid becomes trapped in the valleys minimizing the amount of jetting. In general, impact on a valley yields a lower overall solidification rate than in the case of impact on a crest. This can be explained with the aid of Figs. 8 and 15 by the fact that, in the latter case (Fig. 8), the fluid tends to produce less jetting. When the droplet impacts on the crest, its kinetic energy is significantly reduced by the time it reaches the third crest (when significant jet overflow is first observed) and thus, the amount of jet overflow is reduced. In contrast, when the droplet impacts on a valley (Fig. 15), it has a larger amount of kinetic energy when it reaches the second crest and consequently more fluid overflows and splashes, resulting in a diminished solidification rate. Other cases show a rate of solidification that is proportional to the amount of fluid that is retained in the surface gaps.

Figs. 17 and 18 show the effect of wavelength variation for impact on a valley and should be contrasted with Figs. 11 and 12 for impact on a crest. It is seen that splashing is largely reduced in Fig. 17 in comparison to Fig. 11 due to the fact that the fluid is retained and slowed down in the gap of the substrate (Fig. 17) compared to the fluid speeding down the crest (Fig. 11). The case shown in Fig. 18 shows a peculiar pattern of spreading in comparison to the one shown in Fig. 12. In

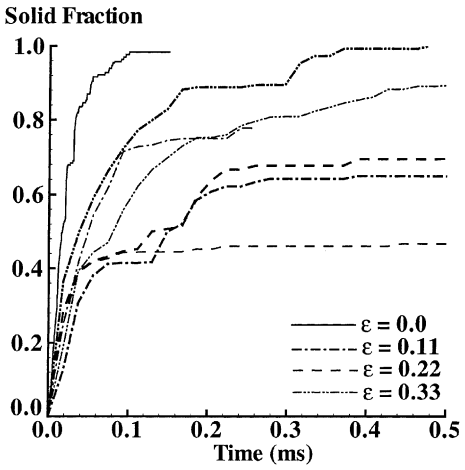

Fig. 16. Effect of the substrate roughness amplitude on the time development of the solid fraction for $\lambda = 0.4$. Thick lines for impact on a crest. Thin lines for impact on a valley.

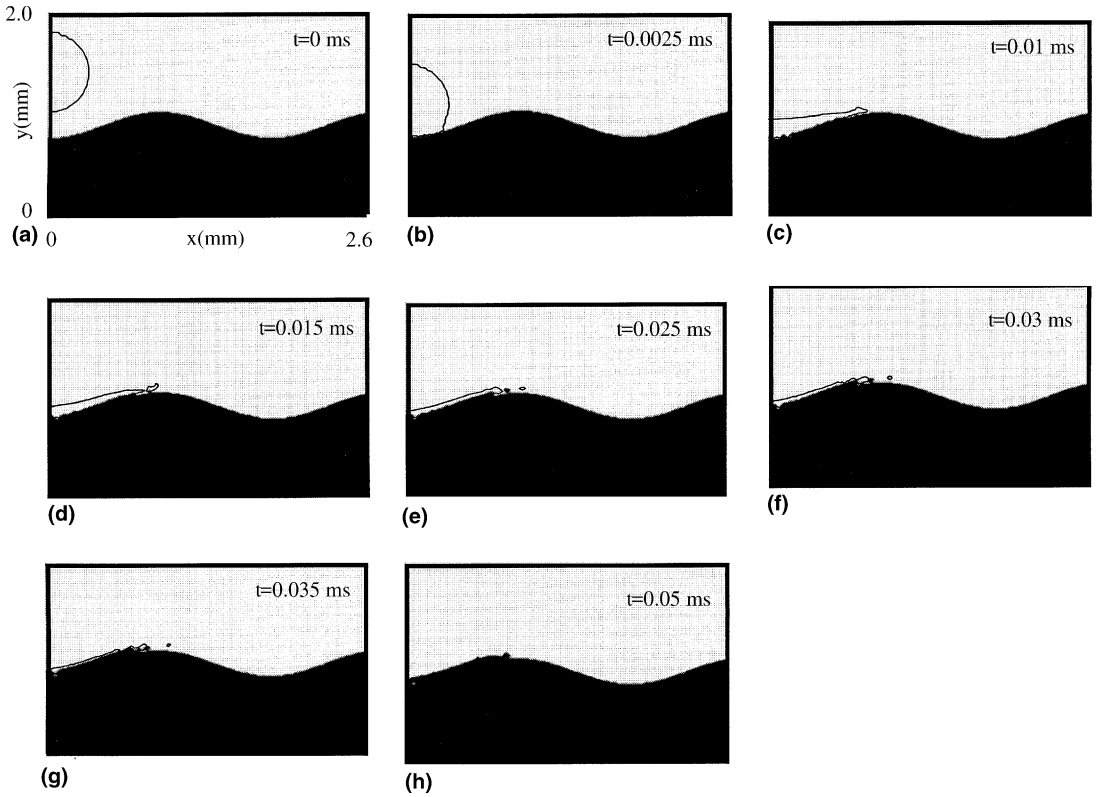

Fig. 17. Time sequence when a 600 μm droplet impinges on the valley of a wavy substrate at a speed of 100 m/s for $\lambda = 2.8$ and $\varepsilon = 0.33$.

Fig. 18, the fluid, after jetting from the first crest, impacts the inner side of the second crest where it jets simultaneously towards the inside and the outside of the valley. Subsequently, the jetted fluid splashes into many satellite blobs, as it is ubiquitous to most of these cases. Fig. 19 compares the rate of solidification for these cases of impact on a valley with those shown in Figs. 8, 11 and 12 for impact on a crest. It is seen that, in contrast to the original cases of impact on a crest, the rate of solidification for impact on a valley increases monotonically with increasing wavelength. This is due to the reduction in the rate of splashing as the wavelength is increased.

Finally, we consider the effect of varying droplet impact velocity. Fig. 20 shows the temporal development of the solid fraction with four different velocities 50, 100, 200 and 400 m/s for impact on a crest with $\lambda = 2.8$ and $\varepsilon = 0.33$. The figure shows the expected trend where the solid fraction is increased as the impact velocity is increased. This is due to the faster rate of droplet spreading. In this regard, the solidification process is qualitatively similar to that on a flat surface.

4. Conclusions

A numerical study of droplet impingement and solidification on molten pools and uneven substrates has been conducted. It is shown that in the case of molten pools, the final morphology of the solidified splat acquires an upward concavity, which increases as the molten pool size increases. Splashing increases as pool size increases due to the increase in available liquid mass that is ejected under the effect of the incoming droplet kinetic energy. As droplet impact velocity increases, the rate of splashing also increases due to the increase in droplet momentum. This finding suggests that, for efficient droplet impingement and bonding on a molten pool, the pool size should be kept small with small impact velocity to reduce the incidence of splashing.

Droplet impingement on an uneven substrate is almost always accompanied by splashing. However, the degree of splashing can decrease with increasing roughness, as more fluid tends to be retained in the surface gaps, where it solidifies. In contrast, droplet impact on substrates with smaller roughness is charac-

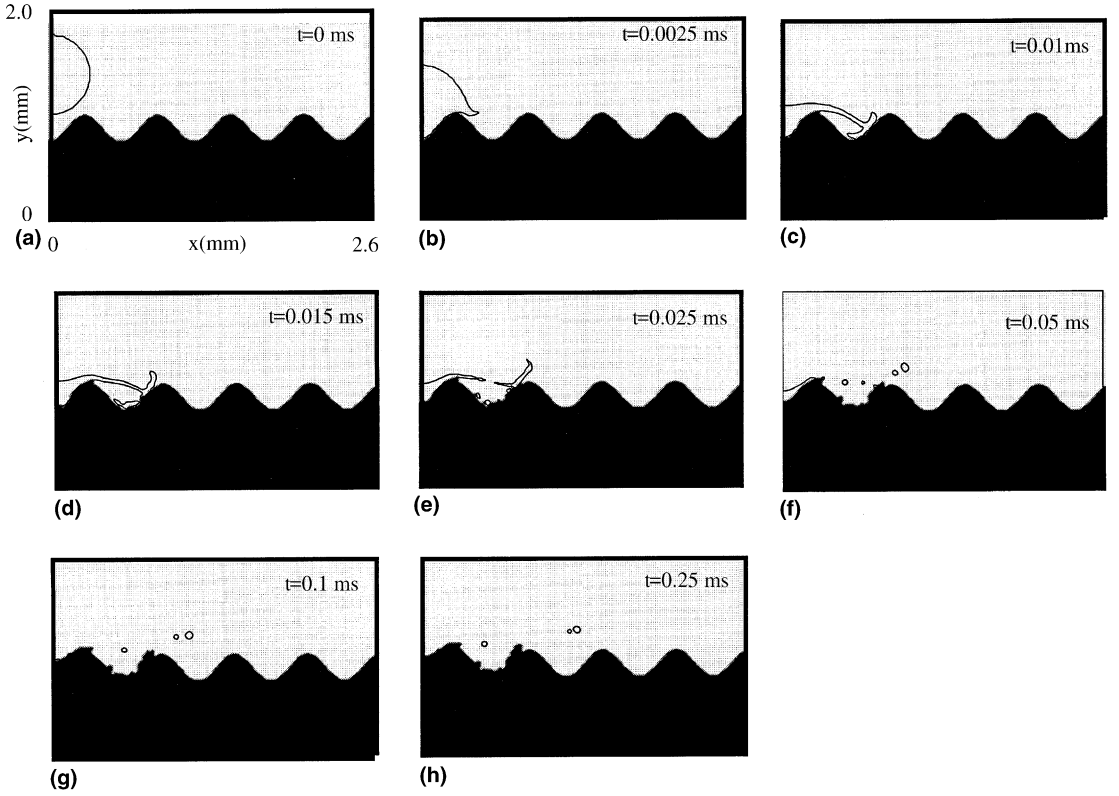

Fig. 18. Time sequence when a 600 μm droplet impinges on the valley of a wavy substrate at a speed of 100 m/s for $\lambda = 0.9$ and $\varepsilon = 0.33$.

terized by more splashing as the liquid tends to jet out under the influence of its momentum. Increasing the substrate wavelength improves droplet spreading and hence solidification. Similarly, increasing droplet impact velocity increases its rate of spreading and also of solidification.

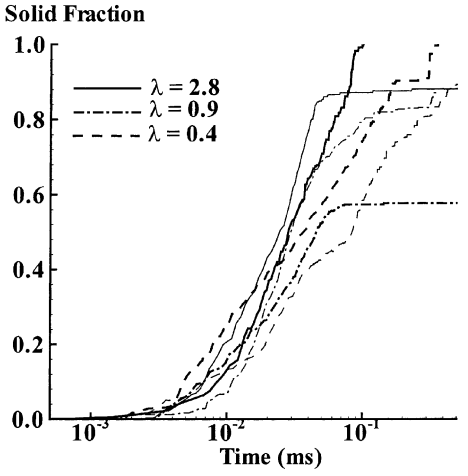

Fig. 19. Effect of the substrate roughness wavelength on the time development of the solid fraction for $\varepsilon = 0.33$. Thick lines for impact on a crest. Thin lines for impact on a valley.

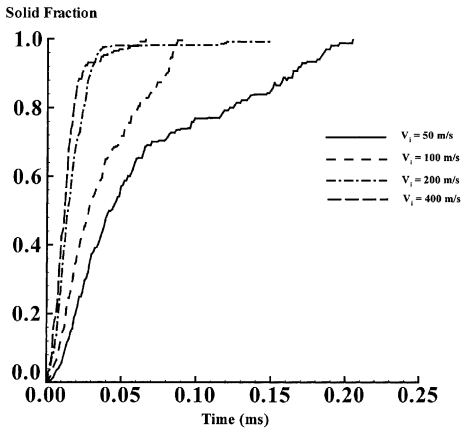

Fig. 20. Effect of varying droplet impact velocity on the time development of the solid fraction for impingement on a crest with $\lambda = 2.8$ and $\varepsilon = 0.33$.

Acknowledgements

This work was supported in part by the National Science Foundation (CTS-9614653), and by a Collaborative University of California Los Alamos National Laboratory (CULAR) research grant.

References

[1] H. Liu, R.H. Rangel, E.J. Lavernia, Modeling of droplet–gas interaction in spray atomization of Ta–2.5W alloy, Mater. Sci. Eng. A 191 (1995) 171–184.

[2] C.H. Amon, K.S. Schmaltz, R. Merz, F.B. Prinz, Numerical and experimental investigation of interface bonding via substrate remelting of an impinging molten metal droplet, Trans. ASME 118 (1996) 164–172.

[3] M. Varadelle, A. Varadelle, A.C. Leger, P. Fauchais, D. Gobin, Influence of particle parameters at impact on splat formation and solidification in plasma spraying processes, J. Thermal Spray Technol. 4 (1994) 50–58.

[4] C. Mundo, M. Sommerfeld, C. Tropea, Droplet–wall collisions: experimental studies of the deformation and breakup process, Int. J. Multiphase Flow 21 (2) (1995) 151–173.

[5] H. Liu, R.H. Rangel, E.J. Lavernia, Modeling of molten droplet impingement on a non-flat surface, Acta Metall. Mater. 43 (2) (1995) 2053–2072.

[6] D.B. Kothe, R.C. Mjolsness, M.D. Torrey, RIPPLE: a computer program for incompressible flows with free surfaces, Technical Report: LA-12007-MS, UC-000, Los Alamos National Laboratory, Los Alamos, NM, 1991.

[7] J.U. Brackbill, D.B. Kothe, C. Zemach, A continuum method for modeling surface tension, J. Comp. Phys. 100 (1992) 335–354.

[8] R.H. Rangel, X. Bian, Metal-droplet deposition model including deformation and substrate remelting, Int. J. Heat Mass Transfer 40 (1997) 2549–2564.

[9] S.V. Patankar, Numerical Heat Transfer and Fluid Flow, Hemisphere, Washington DC, 1980.

[10] J.-P. Delplanque, E.J. Lavernia, R.H. Rangel, Multidirectional solidification model for the description of micropore formation in spray deposition processes, Part A, Numer. Heat Transfer 30 (1996) 1–18.